

## Utilizing top-down hyperspectral imaging for monitoring genotype and growth conditions in maize

Sara B. Tirado<sup>1,2</sup>, Susan St Dennis<sup>2</sup>, Tara A. Enders<sup>3\*</sup>, Nathan M. Springer<sup>2\*</sup>

### Institutional Affiliations:

<sup>1</sup> Department of Agronomy and Plant Genetics, University of Minnesota, Saint Paul, MN 55108

<sup>2</sup> Department of Plant and Microbial Biology, University of Minnesota, Saint Paul, MN 55108

<sup>3</sup> Department of Biology, Hofstra University, Hempstead, NY 11549

\*Co-corresponding authors

ORCID: SBT (0000-0003-0432-091X), NMS (0000-0002-7301-4759), TAE (0000-0002-9634-059X)

### Contact information for corresponding author:

Nathan Springer  
University of Minnesota  
Department of Plant and Microbial Biology  
140 Gortner Laboratory  
1479 Gortner Avenue  
St. Paul, MN 55108  
612-624-6241  
[springer@umn.edu](mailto:springer@umn.edu)

Tara Enders  
Hofstra University  
Department of Biology  
114 Gittleson Hall  
Hempstead, NY 11549  
516-463-8510  
[tara.a.enders@hofstra.edu](mailto:tara.a.enders@hofstra.edu)

Author contributions: SBT, TAE and NMS conceived the experiments; SBT, TAE and SSD conducted the experiments, SBT and TAE conducted the analyses; SBT and NMS wrote the manuscript

Keywords: hyperspectral imaging, plant phenotyping, abiotic stress, maize

Conflict of interest: The authors do not have any conflict of interest to declare.

## 1 **Abstract**

2 There is significant enthusiasm about the potential for hyperspectral imaging to document  
3 variation among plant species, genotypes or growing conditions. However, in many cases the  
4 application of hyperspectral imaging is performed in highly controlled situations that focus on a  
5 flat portion of a leaf or side-views of plants that would be difficult to obtain in field settings. We  
6 were interested in assessing the potential for applying hyperspectral imaging to document  
7 variation in genotypes or abiotic stresses in a fashion that could be implemented in field settings.  
8 Specifically, we focused on collecting top-down hyperspectral images of maize seedlings similar  
9 to a view that would be collected in a typical maize field. A top-down image of a maize seedling  
10 includes a view into the funnel-like whorl at the center of the plant with several leaves radiating  
11 outwards. There is substantial variability in the reflectance profile of different portions of this  
12 plant. To deal with the variability in reflectance profiles that arises from this morphology we  
13 implemented a method that divides the longest leaf into 10 segments from the center to the leaf  
14 tip. We show that using these segments provides improved ability to discriminate different  
15 genotypes or abiotic stress conditions (heat, cold or salinity stress) for maize seedlings. We also  
16 found substantial differences in the ability to successfully classify abiotic stress conditions  
17 among different inbred genotypes of maize. This provides an approach that can be implemented  
18 to help classify genotype and environmental variation for maize seedlings that could be  
19 implemented in field settings.

## 20 **Significance Statement**

21 This study describes the importance of using spatial information for the analysis of hyperspectral  
22 images of maize seedling. The segmentation of maize seedling leaves provides improved

23 resolution for using hyperspectral variation to document genotypic and environmental variation  
24 in maize.

## 25 **Introduction**

26 Abiotic stresses cause major yield declines across many crops and can limit production by up to  
27 70% (Boyer, 1982). Advances in molecular tools have greatly facilitated breeders in efficiently  
28 identifying and selecting germplasm with favorable traits such as tolerance to abiotic stresses;  
29 however, breeders still rely on obtaining high quality phenotypic data for developing and  
30 implementing these methods (Masuka et al., 2012). Phenotyping has become the main bottleneck  
31 in making breeding advances because current methods of phenotyping involve a large amount of  
32 time and labor. This limits their applications across breeding programs which typically consist of  
33 large populations comprised of thousands of lines grown in replicates across multiple  
34 environments (Myles et al., 2009). To effectively breed for tolerance to abiotic stresses,  
35 quantifying the severity of the response to a particular stress across different genotypes as well as  
36 their ability to recover from the stress is crucial. This would require temporal measurements of  
37 phenotypes linked to the stress response which increases the complexity in making progress in  
38 breeding for such traits.

39 The development of high throughput phenotyping tools has taken surge over the last couple of  
40 years to obtain phenotype data quickly and at low costs. Most of these methods rely on remote  
41 sensing techniques that utilize sensors to capture images of plants and subsequently processing  
42 the images to extract meaningful traits. Sensors that measure different ranges of the  
43 electromagnetic spectrum have been applied in agriculture. RGB imaging has been widely used  
44 to extract morphological traits linked to plant productivity across different crop species in field

45 and indoor settings ( Watanebe et al., 2017; Feng et al., 2018; Varela et al., 2017; Enders et al.,  
46 2019). Thermal imaging and near infrared combined with visible imaging have been used to  
47 extract information of drought stress across grasses and legume crops (Martynenko et al., 2016;  
48 Biju et al., 2018; Benavente et al., 2013; Jin et al., 2017; Zhang et al., 2012).

49 More recently, with the advent of advanced machine and deep learning algorithms, multispectral  
50 and hyperspectral sensors that generate large amounts of data at very high spectral and spatial  
51 resolutions have been applied in four key areas in plant phenotyping: identification,  
52 classification, quantification, and prediction of a particular stress (Singh et al., 2015). With  
53 hyperspectral imaging, the user can take advantage of hundreds of spectral channels to uncover  
54 materials and biochemical processes, such as the degradation of pigment molecules and changes  
55 in water content, within plant tissues that can differentiate and potentially quantify differences  
56 across species, genotypes, and stresses. The degradation of pigments such as chlorophyll alters  
57 the amount of reflected, absorbed, and transmitted radiation and can therefore be passively  
58 captured using spectral imaging (Blackburn, 2007).

59 Hyperspectral imaging has been applied for the identification and quantification of several  
60 bacterial and fungal infections including fusarium head blight and leaf rust in wheat (Alisaac et  
61 al., 2019; Mahlein et al., 2019; Qiu et al., 2019; Ashourloo et al., 2014; Bauriegel et al., 2011),  
62 powdery mildew in barley (Thomas et al., 2018), *Cercospora* leaf spot, powdery mildew and leaf  
63 rust in sugarbeet (Mahlein et al., 2012; Rumpf et al., 2010) and *Sclerotinia sclerotiorum* in  
64 oilseed rape plants (Kong et al., 2018). Diseases caused by bacterial or fungal infections tend to  
65 have characteristic features such as bacterial pustules with neighboring chlorotic tissue or  
66 necrotic lesions that are picked up and easily distinguished using spectral imaging. However,

67 identifying more subtle symptoms such as those caused by abiotic stresses can be challenging.  
68 Pandey et al. (2017) found hyperspectral imaging to be useful in quantifying plant leaf chemical  
69 properties that could aid in detecting water and nutrient deficiencies among crops and Obeidat et  
70 al. (2018) discovered that spectral indices correlated with chlorophyll content could help  
71 distinguish between genotypes and cold-stressed plants in indoor settings. Similarly, Behmann et  
72 al. (2014) found that hyperspectral imaging can be used to cluster barley plant pixels into  
73 different levels of drought-stress based on amount of chlorosis and senescence. Also, Römer et  
74 al. (2012) was able to detect drought stress early in development for cereal grains in both indoor  
75 and field settings based on a matrix factorization technique that allows for the computation of  
76 how similar a plant pixel is to the typical spectrum of a healthy plant. Another way to identify  
77 subtle abiotic stress signals using spectral imaging is by correlating reflectance data with other  
78 more laborious, time-consuming or costly measurements correlated to the stress response. Feng  
79 et al (2019) made a link between hyperspectral measurements of okra leaves with measurements  
80 linked to leaf chlorophyll content and fresh weight traditionally used to assess salt stress across  
81 crops.

82 A common problem when analyzing spectral data of plant surfaces is taking into account uneven  
83 light scattering that occurs upon the interaction between incident light and the plant surface being  
84 captured (Makdessi et al., 2017). Plant material possesses non-Lambertian reflectance properties  
85 and plants themselves contain a large amount of morphological variation causing differences in  
86 angle relative to the sensor across leaf segments. Many studies that have evaluated the use of  
87 hyperspectral imaging for assessing plant abiotic stresses have utilized indoor setups with  
88 uniform, nonreflective backgrounds and have dismissed the effects of plant morphology by  
89 securing the plant leaves on a flat background (Obeidat et al., 2018); however, this limits their

90 application in natural settings. Other studies have proposed ways to account for plant  
91 architectural variation. Behman et al. (2015) proposed a method to account for differential light  
92 scattering by performing geometric calibration of hyperspectral cameras that connects a 3D  
93 model with a 2D image and Mohd Asaari et al. (2018) applied a standard normal variate  
94 normalization method to correct spectra for uneven illumination effects. Moghimi et al. (2018)  
95 circumvented plant architectural differences by identifying endmembers indicative of all plant  
96 pixels for a given line in a given treatment and used these to identify salt stress across wheat  
97 lines. Feng et al. (2019), on the other hand, was able to develop an instance segmentation model  
98 using deep learning to segment individual okra plant leaves for further evaluation, which is a  
99 suitable approach for crops where leaves lie relatively flat horizontally with respect to the sensor.

100 Variation in plant architecture across different crops species can make finding a single approach  
101 for analyzing spectra data challenging; however, it can also be taken advantage of in the context  
102 of finding discriminatory patterns within an individual crop. Upon accounting for differences in  
103 light scattering of different plant surfaces, the large number of plant pixels representing single or  
104 multiple individuals are commonly reduced to a single value such as an endmember (Moghimi et  
105 al., 2018) or an average (Mohd Asaari et al., 2018). Looking at all the plant pixels throughout the  
106 plant can elucidate biochemical processes in response to certain stimuli that vary spatially  
107 throughout a plant. This spatial variation could be useful for identifying more subtle symptoms  
108 that may be masked out by reducing the data to a single value per line or treatment or by  
109 normalizing the data to account for scattered light due to differences in plant morphology.

110 Moreover, although multiple studies have identified indices that are useful for a particular stress,  
111 they have not looked into how these would change due to plant morphology. This study aims to  
112 elucidate the effects of morphology and stress on the spatial variation of reflectance values

113 within plant leaves and compare the ability of reflectance data for different regions of the leaf to  
114 resolve genetic and environmental factors relative to reflectance data for the entire plant.  
115 Currently, this remains unknown and could enlighten new mechanisms for identifying,  
116 classifying, quantifying and predicting the onset and recovery of biotic and abiotic stresses where  
117 little variation is observed with the naked eye.

## 118 **Results and discussion**

119 In most field settings, hyperspectral images of cereal crops are collected from above, resulting in  
120 a top-down view of the plants. We sought to develop approaches for the analysis of hyperspectral  
121 images for maize plants that could be applicable to field settings. We obtained raw intensity data  
122 using a top-down approach for wavelengths ranging from approximately 400 to 1000 nm for  
123 several controlled-condition experiments. The experiments contained maize seedlings of multiple  
124 inbred genotypes subjected to different environmental treatments. Plants were illuminated by  
125 halogen lights, which are oriented in two parallel rows of bulbs on either side of the camera and  
126 each image contained 3 plants (Figure S1). Raw intensity values for the resulting images of  
127 plants were converted to reflectance using white and dark references and then normalized by  
128 their L2 norm (see methods). For each plant, the NDVI values were utilized to identify pixels  
129 containing plant tissue and thresholded to generate a binary image mask to extract the reflectance  
130 values at each wavelength for entire plants.

131 This approach was applied to several different experiments that are summarized in Table S1. We  
132 sought to address different themes in our analyses of this data. First, different genotypes or  
133 environments often result in changes in plant morphology (Enders et al., 2019). We evaluated the  
134 potential of hyperspectral data to capture morphological differences by utilizing changes in

135 reflectance for specific regions of a plant. In our analyses, we compared the ability of using  
136 whole plant data relative to using specific regions of leaves in the ability to resolve genetic or  
137 environmental factors. Second, hyperspectral imaging provides opportunities to identify genetic  
138 or environmental variation. We assessed the relative ability of using hyperspectral imaging data  
139 to accurately classify environmental conditions in different genotypes using machine-learning  
140 approaches. To achieve these goals, we collected hyperspectral data using the described system  
141 for two experiments. The first experiment (E1) consists of three replicates of five genotypes of  
142 maize seedlings under four treatment groups (control, cold, salt, and heat) imaged at a single  
143 time point. The chosen genotypes were previously demonstrated to differ in responses to cold  
144 stress (Enders et al.,2019). The second experiment (E2) consists of two genotypes under four  
145 treatment groups (control and three severities of salt stress) imaged at three timepoints  
146 (immediately before the stress, 2 days following the stress treatment, and 4 days after following  
147 the stress treatment). A total of 540 plant images are represented in the dataset. We have used the  
148 dataset to address a series of questions about the ability of hyperspectral imaging to resolve the  
149 effects of growth stage, genotype and various abiotic stresses across portions of maize leaves.

#### 150 *Spatial variation in top-down images of seedlings*

151 The system and approach that was used to generate images of maize seedlings results in a  
152 relatively large number of pixels (1,908-13,831) for each plant. These pixels exhibit a range of  
153 reflectance values with substantial standard deviation (Figure S2). A top-down image of a maize  
154 seedling consists of a central whorl from which leaves extend. The whorl has a funnel-like shape  
155 with each leaf extending in an arc (Figure 1A). Given the variation in reflectance based on the  
156 orientation of the plant surface relative to the lights and camera, there is substantial variability in

157 reflectance from the central whorl to the leaf blade tip. In addition, there is biological variation in  
158 gene expression and physiological properties of leaves from the base to the tip (Li et al., 2010).  
159 We sought to compare the average normalized reflectance values from each plant within zones  
160 extracted along the length of a leaf. To classify relatively consistent zones of a plant leaf, we  
161 implemented an approach to divide the longest leaf into ten sections and identify the plant pixels  
162 within each section (Figure 1, see methods for details). This resulted in a set of 10 segments that  
163 were used as a mask for the hyperspectral image cube to extract normalized reflectance values by  
164 leaf zone.

165 The average reflectance profiles and variance were compared for the entire leaf relative to each  
166 of the ten leaf sections. Substantial variability is observed in pixel counts across leaf segments  
167 due to differences in width across the length of the leaf (Figure 1). While the overall pattern of  
168 reflectance values is generally similar among plant segments there is substantial variability  
169 within and across plant segments for the magnitude of specific patterns. In many cases the  
170 variation in spectral profiles across leaf segments can be difficult to visualize when using the  
171 reflectance patterns for the entire spectrum (Figure 1B). PCA of the reflectance values for each  
172 segment of each plant suggests differences in the most outer segments of the leaves relative to  
173 more central regions of the leaf (Figure 2A). A comparison of the reflectance profiles across leaf  
174 segments focused only on the visible range of the spectrum reveals distinct reflectance profiles  
175 between leaf segments near the center or leaf tip relative to the middle portion of the leaf in both  
176 Mo17 and PH207 (Figure 2B).

177 We selected three representative wavelengths in the red, green, and blue range of the light  
178 spectrum (625 nm, 550 nm, and 498 nm; Figure 2B) and assessed the distribution of average

179 reflectance values for all plants for each of the leaf segments as well as the entire leaf (Figure  
180 2C). For several of the segments the reflectance values for these three wavelengths exhibit  
181 distributions of values that are significantly different from each other or from the entire leaf  
182 (Figure 2D). In general, the patterns are similar for the two genotypes. Relative to the values  
183 observed for the entire leaf there are often significant differences in the distribution of values  
184 seen from the middle and the tip of the leaf. The tip of the leaf is often distinct from many other  
185 zones as well. These observations highlight the variability throughout a single leaf and suggest  
186 that using all values for a plant or leaf will likely obscure spatial variation that may occur due to  
187 developmental, genetic or environmental factors.

#### 188 ***Stable patterns of hyperspectral signal for different stages of seedling growth***

189 The differences in hyperspectral profiles were assessed for PH207 seedlings grown in control  
190 conditions that were 11, 13 and 15 days after sowing to document whether there are differences  
191 as seedlings mature and whether the differences among leaf segments are consistent over time  
192 (Figure 3). PCA reveals that differences across leaf segments account for most of the observable  
193 variation in reflectance intensity compared to differences observed between days (Figure 3A).  
194 Across the three time points, average reflectance values cluster into groups corresponding to leaf  
195 segments near the leaf tip, leaf segments towards the middle of the leaf, and leaf segments  
196 towards the center whorl. No clustering by date was observed even though plant size and  
197 morphology changes were observed based on trait data obtained from RGB images (Figure S3,  
198 see methods). The profiles of reflectance values are slightly different on the three dates (Figure  
199 3B) but the distribution patterns for the different leaf segments relative to each other remain  
200 consistent. Examination of the distribution of values at three wavelengths reveals similar

201 distributions for plants at the three dates and similar trends among the different leaf segments  
202 (Figure 3C).

### 203 *Ability to distinguish genotypes using hyperspectral imaging*

204 Hyperspectral profiling has been widely used for separating different plant species such as weeds  
205 (Pantazi, Moshou and Bravo, 2016) and tropical forest trees (Laybros et al., 2019). Fewer studies  
206 have used hyperspectral profiling to separate different genotypes or lines of the same species. A  
207 study by Obeidat et al. (2018) showed that genotype main effects across short-season maize lines  
208 significantly contributed to variation in various spectral reflectance indices as well as spectral  
209 reflectance in the visible and near-infrared range when comparing hyperspectral scans of flat  
210 leaves. This variation, particularly in the spectral reflectance across the visible range of the  
211 spectrum, was likely due to chlorophyll and carotenoid differences (Obeidat et al., 2018). To  
212 assess variation in spectral reflectance among maize genotypes, we applied our leaf segmentation  
213 approach to compare the reflectance values across individual leaf segments among the different  
214 inbred lines grown in control conditions in experiment E1. Experiment E1 consisted of images  
215 from 9 plants for five different genotypes. While the overall average profiles for the entire leaf  
216 are relatively similar in the visible range, there are some leaf segments that show more  
217 pronounced differences among genotypes (Figure 4A). In particular, MS71 shows higher  
218 reflectance for wavelengths near 550 nm for central segments of the leaf but lower reflectance  
219 compared to other genotypes for wavelengths near 500 nm and 675 nm for segments near the  
220 leaf tip. However, these differences are reduced in averages that include all pixels for the entire  
221 leaf (Figure 4A).

222 To further evaluate whether specific leaf segments can be more useful than whole leaves in  
223 distinguishing individual genotypes, we developed a cubic support vector machine (SVM) model  
224 utilizing  $\frac{1}{3}$  of all the pixel values from all plants grown in control conditions in experiment E1 to  
225 predict the corresponding genotype. The predictor variables included normalized reflectance  
226 values for wavelengths in the visible range as well as the leaf segment of the corresponding  
227 pixel. We then applied this model to predict the genotype of the remaining  $\frac{2}{3}$  pixel values in the  
228 dataset. This included pixels from all leaf segments. The proportion of pixels per plant that were  
229 classified into each genotype for each of the zones of each maize line was determined (Figure  
230 4B). The model is able to correctly identify MS71 pixels in most leaf segments although the  
231 accuracy is somewhat lower in the whorl region (Figure 4B). The other genotypes are less  
232 accurately identified. B73 is most accurately identified for the central leaf segments but is often  
233 confused with Ki11 (Figure 4B). PH207 and Mo17 generally exhibit relatively low correct  
234 prediction accuracies throughout the leaf and are frequently mis-classified as B73 or Ki11  
235 (Figure 4B).

### 236 *Ability to distinguish and quantify abiotic stresses using hyperspectral imaging*

237 Two different experiments were performed to investigate the potential to utilize hyperspectral  
238 profiling for documenting the effects of abiotic stress on maize seedlings. For experiment E2 we  
239 treated two genotypes, Mo17 and PH207, with three different concentrations of salt applied on  
240 day 11 immediately after imaging (Figure 5A). These plants were then imaged two and four days  
241 after the stress application. Two cubic SVM models were developed using  $\frac{1}{3}$  of all pixels from  
242 the control and the medium salt stress treatment groups. In both models, the treatment (Control  
243 or 0.75M NaCl) was the response variable. The first model was trained using pixels randomly

244 selected throughout the entire plant; however, the second model only contained pixels randomly  
245 selected from the longest leaf. In the first model, the normalized reflectance values for  
246 wavelengths in the visible range, the genotype, and the day of imaging represented as days after  
247 sowing (DAS) were set as the predictor variables. In the second model, the corresponding leaf  
248 segment was also included as a predictor variable. Moreover, the first model was used to predict  
249 all the pixels from entire plants in the E2 dataset from all treatment groups into belonging to the  
250 control or salt stressed class (Figure 5B). On the other hand, the second model was used to  
251 predict all pixels from the longest leaf of all plants (Figure 5C).

252 As expected, the proportion of pixels classified as salt-stressed was not different for the control  
253 and the treatment groups at day 11 for either model as these images were collected prior to the  
254 actual stress treatment application (Figure 5B; Figure 5C). However, at day 13 and day 15, two  
255 and four days after application of salt we see substantial increases in the proportion of pixels  
256 classified as salt stressed (Figure 5B; Figure 5C). When looking at the classifications based on  
257 the entire plant using the first model, the proportion of pixels classified as salt stressed increases  
258 at higher concentrations of salt treatment and is higher at day 15 than at day 13 (Figure 5B).  
259 However, there are a high frequency of pixels in control plants classified as salt stressed in this  
260 analysis. A comparison of the predictive ability for different leaf segments revealed substantial  
261 variation across the leaf. At days 13 and 15 the segments from the middle of the leaf have higher  
262 correct prediction accuracy than segments near the leaf tip or whorl (Figure 5C). Importantly,  
263 these mid-leaf segments also outperform the predictions based on using the entire plant. A  
264 relatively small proportion of pixels from control plants are classified as stressed in these mid-  
265 leaf segments while the majority of pixels in plants with 0.75M or 1M NaCl treatment are  
266 classified as stressed.

267 Experiment E1 included five genotypes treated with four conditions including control, heat  
268 stress, cold stress and salt stress and plants were imaged after two days of the stress treatment.  
269 Visual examination of the plants revealed differences in severity of stress response for the  
270 different genotypes (Figure S4). This is quantified for cold stress by Enders et al (2019). For  
271 example, Ki11 tends to have strong responses, especially to cold and salt stress while Mo17 has  
272 minimal visual responses to the stresses (Figure S4). The average hyperspectral profiles for the  
273 entire leaf reveal limited changes for Mo17 but some differences for Ki11 (Figure 6A). The  
274 differences in hyperspectral profiles for the different treatments were more severe in some leaf  
275 segments compared to others (Figure 6A). A cubic SVM model was developed to predict the  
276 treatment using predictor variables of normalized reflectance values, genotype, and leaf segment.  
277 The proportion of pixels classified into each condition is shown for each segment of each actual  
278 treatment (Figure 6B, C). For Ki11 there is a high true prediction accuracy for cold and salt  
279 stress across all segments of the plants; however, the prediction accuracy is further improved for  
280 segments near the middle of the leaf for cold stress and the tip of the leaf for salt stress (Figure  
281 6B). Heat stress is not predicted as accurately with substantial confusion between control and  
282 heat stress (Figure 6B). This likely reflects minimal phenotypic response to heat stress for Ki11.  
283 Similar patterns of enhanced prediction accuracy utilizing middle segments of the leaf compared  
284 to the entire leaf across treatments are also observed for the other four genotypes (Figure S5, S6).

285 If we compare the accuracies of a representative leaf segment in the center whorl, the middle  
286 portion of the leaf, the tip of the leaf, and the entire leaf in predicting the abiotic stress response  
287 across genotypes, we observe differences in utility of different leaf segments based on the stress  
288 being predicted as well as the genotype (Figure 6C). Leaf segments in the middle portion of the  
289 leaf as well as the leaf tip provided the highest true prediction accuracy overall across treatments

290 and genotypes compared to the center whorl and utilizing all segments from the leaf. Leaf  
291 segments towards the middle portion of the leaf (segment 6 in this case) provide a higher  
292 prediction accuracy across most genotypes for predicting cold stress and across some genotypes  
293 (Mo17, MS71 and PH207) for salt stress; however, the leaf tip was more informative for heat  
294 stress and across some genotypes such as Ki11 for salt stress (Figure 6C). Overall, most pixels  
295 that were misclassified across genotypes and treatments were predicted to belong to the control  
296 treatment group.

## 297 **Conclusions**

298 Hyperspectral profiling provides new opportunities for optical analysis of trait variation in crops.  
299 Many studies have reported the ability to monitor physiological changes in plants using point  
300 profiles of reflectance from a single region of a leaf (Meacham-Hensold et al., 2019; Silva-Perez  
301 et al., 2018; Smith et al., 2004; Yendrek et al., 2017). However, there has been less analysis of  
302 the ability to separate effects of genotype or environmental conditions using whole plant images.  
303 In this study we highlight the potential for using hyperspectral imaging but also show that using  
304 averages of whole plants provides less resolution than focusing on specific regions of plants. The  
305 variation in spectral profiles from the base of the leaf to the tip of the leaf likely represents a  
306 combination of physiological differences as well as variation in the plant shape/leaf angle  
307 resulting in differing reflectance. In this study, we have not separated these factors but instead  
308 have simply relied upon segmentation of the leaf to reduce variance and improve discrimination.  
309 There are several limitations to our approach for segmenting the longest leaf and making  
310 comparisons of specific leaf segments across dates, genotypes and treatments. In this work, we  
311 performed manual detection of the center of the plant and the remainder of the leaf identification

312 and segmentation process was automated. It is likely that spectral properties or plant shape could  
313 be used for automated detection of the center of the whorl. Additionally, when comparing leaf  
314 segments for varying genotypes or growing conditions the length of the longest leaf may vary as  
315 plants exhibit different growth rates for different stress conditions or among genotypes. This  
316 results in differing numbers of pixels for the segments being compared. However, since we are  
317 segmenting into 10 equally sized regions the relative segmentation of the leaf should remain  
318 consistent. Another potential issue is the variation in the angle of the leaf tip. As a leaf emerges  
319 from the whorl it has an upright angle. As the leaf extends the tip will shift from upright to  
320 horizontal to having a downward angle. There is biological variation among plants at the same  
321 developmental stage for the angle of the leaf tip. This may result in increased variance for  
322 segments near the leaf tip, as noted in our PCA plots (Figure 2A, 3A). However, many stress  
323 conditions have visible effects on the leaf margins near the leaf tip and this region provided the  
324 best classification for some stresses. One additional potential complication is the presence of  
325 mixed pixels that include some plant tissue as well as background. We implemented relatively  
326 strict cutoffs to minimize the number of mixed pixels obtained after plant segmentation but there  
327 are likely a small number of mixed pixels captured in our plant masks. These may be represented  
328 in uneven quantities across leaf segments with more mixed pixels appearing in narrower  
329 segments such as the leaf tip relative to the base of leaf.

330 Our findings highlight the utility of plant segmentation for improved accuracy of genotype or  
331 environment predictions using hyperspectral data. It is worthwhile to note that there is not a  
332 single region of the leaf with the highest performance. Instead the most accurate regions varied  
333 for different stresses or genotypes. The use of wider panels of genotypes would likely result in  
334 classification of groups with similar behaviors, but in this study we focused on improving the

335 methods for stress detection in a small set of variable genotypes. Our classification prediction  
336 rates vary substantially. This is likely due to variation among the genotypes. Some genotypes are  
337 more tolerant of certain abiotic stresses and we can observe a higher proportion of pixels  
338 misclassified into the control classes for these. In contrast, genotypes that are more sensitive to a  
339 certain stress exhibit a larger prediction accuracy for stress prediction for the particular  
340 treatment. The approaches of segmenting leaves for hyperspectral analysis can likely be  
341 conducted for larger scale field experiments and may improve the utility of hyperspectral profiles  
342 for documenting genotype, environment and genotype by environment effects.

## 343 **Methods**

### 344 ***Plant growth***

345 Two experiments were conducted, E1 and E2 (Table S1). For all experiments, seeds were  
346 planted approximately 2 inches below the surface in 40 cubic inch D $\times$ 40 DeePots (Stuewe and  
347 Sons, Inc.) containing a 1:1 mix of SunGro (Agawam, MA) horticulture professional growing  
348 mix and autoclaved field soil. All plants were grown in Conviron growth chambers with a 16 hr  
349 30°C and 8 hr 20°C day/night cycle and watered every other day.

350 In experiment E1, five maize genotypes (B73, Mo17, PH207, Ki11, MS71) were subjected to  
351 four treatment conditions (control, cold, heat, salt). Plants for all treatments were grown in  
352 control conditions until 11 DAS when the stresses were applied for the cold, heat and salt  
353 treatments. The cold $\square$ stress treatments were implemented using a Thermo Scientific refrigerated  
354 incubator programmed with a 16 hr 6°C and 8 hr 2°C day/night cycle and applied for 48 hours.  
355 The heat $\square$ stress treatments were implemented using a Thermo Scientific refrigerated incubator

356 programmed with a 16 hr 39°C and 8 hr 29°C day/night cycle and applied for 48 hours. The salt  
357 stress was a single 50 mL 0.75 M NaCl treatment at Zeitgeber Time 2 (ZT2) at 11 DAS. Plants  
358 were imaged with our hyperspectral and RGB imaging systems at the end of the stress treatment  
359 at ZT2 at 13 DAS. Three experimental replicates were grown each consisting of three plants per  
360 genotype per treatment condition, for a total of 9 plants per genotype per treatment.

361 Experiment E2 consisted of two maize genotypes (Mo17 and PH207) subjected to four treatment  
362 conditions (control, low salt, medium salt and high salt stress). The low, medium and high salt  
363 stress treatments were implemented by a single 50 mL 0.5 M NaCl, 0.75 M NaCl or 1 M NaCl  
364 treatment, respectively, at ZT2 at 11 DAS. Plants were imaged with our hyperspectral and RGB  
365 imaging systems before undergoing stress at ZT2 at 11 DAS, at the end of the stress treatment at  
366 ZT2 at 13 DAS and two days after the stress treatment at 15 DAS. The experiment consisted of  
367 15 plants per genotype per treatment.

### 368 *Hyperspectral image acquisition*

369 To capture the hyperspectral images, a custom-built line-scanning system from Middleton  
370 Spectral Vision (Madison, WI) was utilized (Figure S1). The system contains a Specim V10  
371 spectrograph with a spectral range of 400 to 1000 nm and approximately a 1 nm spectral  
372 resolution. The spectrograph was mounted on an Imperx IPX-2M30 camera with 1600x1200  
373 pixel spatial resolution. When acquiring hyperspectral images, a spectral binning of 2x was  
374 applied to obtain an average spectral resolution of 2.3nm.

### 375 *Hyperspectral Data Pre-processing and Normalization*

376 Black and white references are gathered by capturing and averaging 10 hyperspectral frames  
377 with the camera shutter closed and for a white lambertian reference panel each date of data  
378 collection. Intensity values for each pixel at each wavelength are converted to reflectance values  
379 by subtracting the dark reference and dividing the result by the difference between the white and  
380 dark references (Yoon and Park, 2015). The resulting reflectance values are then normalized by  
381 dividing each spectrum by its L<sub>2</sub> norm, or the square root of the sum of the squares of that  
382 signature, following the equation

$$x_{norm} = \frac{x}{\sum_{i=1}^n (x_i^2)^{1/2}}$$

383 where  $x$  is the full vector of reflectance data in image,  $i$  is the response band,  $n$  is the total  
384 number of measured wavelengths and  $x_i$  is the full vector of reflectance data in image for the  
385 response band  $i$ .

### 386 ***Segmenting Plant Material and Longest Leaf into Individual Segments***

387 All approaches for identifying, segmenting and extracting data from leaf segments were  
388 implemented utilizing custom MATLAB algorithms (MATLAB, 2018a). Plant material was  
389 segmented by calculating the NDVI value of each pixel and thresholding to a value of 0.35 or  
390 greater to create a binary plant segmentation mask. This threshold was found to balance  
391 maintaining the highest percentage of plant pixels while minimizing the number of mixed pixels  
392 in the extracted data. Each hyperspectral image contained three plants of the same genotype and  
393 treatment in a defined location. Individual plant objects were identified from the plant material  
394 mask using the *bwconncomp* function in MATLAB which returns connected components with a  
395 connectivity of 8 (MATLAB, 2018b). Objects caused by background noise were then removed

396 by only keeping objects that had a minimum of 1,000 pixels and a maximum of 3,000 pixels and  
397 allocated an ID (plant A, B or C) based on their location in the image.

398 For each plant (plant A, B and C) of each image, the approximate center of the leaf whorl was  
399 identified by manually identifying the x-y coordinates of the plant center from an NDVI  
400 grayscale representation. This represented the only manual input in the pipeline. Extrema of the  
401 plant object were then automatically identified using the *regionprops* function in MATLAB  
402 (MATLAB, 2018b). Using the x-y coordinates for each terminal extrema and whorl center, the  
403 extrema farthest away from the center was identified for each plant representing the tip of the  
404 longest leaf. The distance of the center to the longest leaf tip was then divided into ten  
405 equidistant points in linear space and 10 concentric rings were generated utilizing the identified  
406 distance between points as the radius (Figure 1A). Each ring segment was used as a mask  
407 coupled with the plant material segmentation mask to extract leaf segments along the plant  
408 (Figure 1A). To ensure that only segments belonging to a single, constant leaf were kept, only  
409 segments that also overlapped with a straight line that extended from the center of the plant to  
410 the longest leaf tip were kept. Each of these ten segments were used as a mask for the  
411 hyperspectral image cube, and reflectance data was extracted for wavelengths 420 nm to 1000  
412 nm after trimming off noisy wavelengths. The reflectance values of each pixel in the plant were  
413 then normalized by the L2-norm calculated on a whole image basis for each wavelength (see  
414 Hyperspectral Data Pre-processing and Normalization methods section). This normalized data  
415 was then exported for further analysis.

416 ***Outlier Detection and Removal***

417 Individual leaf segments for each plant were visually assessed by looking at the leaf segment  
418 binary masks and all data from the given segment excluded in the analysis if the segment  
419 encompassed multiple leaves (which happened in cases where part of the given segment was  
420 close to the whorl before leaves separated or when leaves overlapped each other), if the leaf  
421 segment had less than 25 pixels, or if the segment was not on the primary longest leaf (which  
422 occurred in some cases where the leaf curled or overlapped another leaf). A total of 156 plants of  
423 the entire 540 had at least one leaf segment excluded (29%); however, the final number of leaf  
424 segments excluded was 187 out of the total 5400 (3%). The majority of excluded segments were  
425 located adjacent to the whorl in cases where the leaves were short and the second leaf segment  
426 encompassed multiple leaves.

#### 427 ***Prediction Model Development and Implementation***

428 All cubic support vector machine (SVM) models were developed using the Classification  
429 Learner application in MATLAB with specified response and predictor variables (MATLAB,  
430 2018c). Cubic SVM models were selected after testing 13 different machine learning algorithms  
431 as these models consistently provided the highest prediction accuracy across the different  
432 applications specified in this study. A random subsampling of 1/6th of all pixels from all plants  
433 in the target dataset was used as the training dataset to create the model (Figure S7). Five-fold  
434 cross-validation was utilized to evaluate the performance of the algorithm during model building  
435 to prevent model overfitting during training (Figure S7). This involved further randomly  
436 partitioning the data into a testing and training set five times. The training sets were used to train  
437 the supervised learning algorithm and the testing sets were used to obtain an average cross-  
438 validation error estimate to evaluate the algorithm performance. Each trained cubic SVM model

439 was then exported and used to predict response classes for remaining 5/6th of pixels constituting  
440 the validation set and obtain prediction accuracy estimates (Figure S7).

#### 441 ***Statistical Analyses***

442 The average spectra for each leaf segment of each plant was compared to the average spectra of  
443 each other segment as well as the average spectra for the entire leaf and the entire plant to assess  
444 which leaf segments significantly differ from each other. The comparisons were made by  
445 performing a pairwise Wilcoxon Rank Sum Test between all pairwise comparisons of leaf  
446 segments using the pairwise.wilcox.test function from the R stats package (R Core Team, 2012).

#### 447 ***RGB Trait Data Acquisition***

448 RGB side-view images of each set of plants were collected immediately following hyperspectral  
449 data collection using the procedures specified in Enders et al. (2019).

450 The scripts and processes used to perform the data normalization and leaf segmentation are  
451 available at [https://github.com/SBTirado/HS\\_LeafSegmentation.git](https://github.com/SBTirado/HS_LeafSegmentation.git).

#### 452 **Acknowledgements**

453 This work was supported by the National Science Foundation Plant Genome Award IOS-  
454 1444456.

#### 455 **References**

456 Alisaac, E., Behmann, J., Rathgeb, A., Karlovsky, P., Dehne, H., Mahlein, A. (2019).  
457 Assessment of Fusarium Infection and Mycotoxin Contamination of Wheat Kernels and Flour

- 458 Using Hyperspectral Imaging. *Toxins*, 11(10). doi: 10.3390/toxins11100556
- 459 Ashourloo, D., Mobasheri, M.R., Huete, A. (2014) Evaluating the Effect of Different Wheat Rust  
460 Disease Symptoms on Vegetation Indices Using Hyperspectral Measurements. *Remote Sensing*,  
461 6(6). doi: 10.3390/rs6065107
- 462 Bauriegel, E., Giebel, A., Geyer, M., Schmidt, U., Herppich, W.B. (2011) Early detection of  
463 Fusarium infection in wheat using hyper-spectral imaging. *Computers and Electronics in*  
464 *Agriculture*, 75(2), 304-312. doi: 10.1016/j.compag.2010.12.006
- 465 Behmann, J., Mahlein, A., Paulus, S., Kuhlmann, H., Oerke, C., Plümer, L. (2015) Calibration of  
466 hyperspectral close-range pushbroom cameras for plant phenotyping. *ISPRS Journal of*  
467 *Photogrammetry and Remote Sensing*, 106, 172-182. doi: 10.1016/j.isprsjprs.2015.05.010
- 468 Behmann, J., Schmitter, P., Steinrücken, J., Plümer, L. (2014) Ordinal classification for efficient  
469 plant stress prediction in hyperspectral data. *Int. Arch. Photogramm. Remote Sens. Spatial Inf.*  
470 *Sci.*, XL-7, 29-36. doi:10.5194/isprsarchives-XL-7-29-2014
- 471 Benavente, E., García-Toledano, L., Carrillo, J.M., Quemada, M. (2013) Thermographic  
472 Imaging: Assessment of Drought and Heat Tolerance in Spanish Germplasm of Brachypodium  
473 Distachyon. *Procedia Environmental Sciences*, 19, 262-266. doi: 10.1016/j.proenv.2013.06.030
- 474 Biju, S., Fuentes, S., Gupta, D. (2018) The use of infrared thermal imaging as a non-destructive  
475 screening tool for identifying drought-tolerant lentil genotypes. *Plant Physiol Bioschem*, 127, 11-  
476 24. doi: 10.1016/j.plaphy.2018.03.005
- 477 Blackburn, G.A. (2006) Hyperspectral remote sensing of plant pigments. *Journal of*

- 478 *Experimental Botany*, 58(4), 855-867. doi: 10.1093/jxb/erl123
- 479 Boyer, J.S. (1982) Plant Productivity and Environment. *Science*, 218(4572), 443-448. doi:  
480 10.1126/science.218.4571.443
- 481 Enders, T.A., St. Dennis, S., Oakland, J., Callen, S.T., Gehan, M.A., Miller, N.D., Spalding,  
482 E.P., Springer, N.M., Hirsch, C.D. (2019) Classifying cold stress responses of inbred maize  
483 seedlings using RGB imaging. *Plant Direct*, 3(1). doi: 10.1002/pld3.104
- 484 Feng, A., Sudduth, K.A., Vories, E.D., Zhang, M., & Zhou, J. (2018) Cotton Yield Estimation  
485 based on Plant Height From UAV-based Imagery Data.2018 ASABE Annual International  
486 Meeting. doi: 10.13031/aim.201800483.
- 487 Feng, X., Zhan, Y., Wang, Q., Yang, X., Yu, C., Wang, H., Tang, Z., Jiang, D., Peng, C., He, Y.  
488 (2019) Hyperspectral imaging combined with machine learning as a tool to obtain high-  
489 throughput plant stress phenotyping. *The Plant Journal*. doi:10.1111/tpj.14597
- 490 Jin, X., Shi, C., Yu, C.Y., Yamada, T., Sacks, E.J. (2017) Determination of Leaf Water Content  
491 by Visible and Near-Infrared Spectrometry and Multivariate Calibration in Miscanthus.  
492 *Frontiers in Plant Sciences*, 8: 721. doi: 10.3389/fpls.2017.00721
- 493 Kong, W., Zhang, C., Huang, W., Liu, F., He, Y. (2018) Application of Hyperspectral Imaging  
494 to Detect *Sclerotinia sclerotiorum* on Oilseed Rape Stems. *Sensors*, 18(1), 123. doi:  
495 10.3390/s18010123
- 496 Laybros, A., Schläpfer, D., Féret, J., Descroix, L., Bedeau, C., Lefevre, M., Vincent, G. (2019)  
497 Across Date Species Detection Using Airborne Imaging Spectroscopy. *Remote Sensing*, 11(7),

498 789. doi: 10.3390/rs11070789

499 Li, P., Ponnala, L., Gandotra, N., Wang, L., Si, Y., Tausta, S.L., Kebrom, T.H., Provart, N.,

500 Patel, R., Myers, C.R. (2010) The developmental dynamics of the maize leaf transcriptome.

501 *Nature Genetics*, 42(12), 1060-1067. doi:10.1038/ng.703

502 Mahlein, A., Alisaac, E., Al Masri, A., Behman, J., Dehne, H., Oerke, E. (2019) Comparison and

503 Combination of Thermal, Fluorescence, and Hyperspectral Imaging for Monitoring Fusarium

504 Head Blight of Wheat on Spikelet Scale. *Sensors*, 19(10), 2281. doi: 10.3390/s19102281

505 Mahlein, A., Steiner, U., Hillnhütter, C., Dehne, H., Oerke, E. (2012) Hyperspectral imaging for

506 small-scale analysis of symptoms caused by different sugar beet diseases. *Plant Methods*. 8:3.

507 doi:10.1186/1746-4811-8-3

508 Makdessi, N., Jean, P., Ecartot, M., Gorretta, N., Rabatel, G., Roumet, P. (2017) How plant

509 structure impacts the biochemical leaf traits assessment from in-field hyperspectral images: A

510 simulation study based on light propagation modeling in 3D virtual wheat scenes. *Field Crops*

511 *Research*. 205, 95-105. doi: 10.1016/j.fcr.2017.02.001

512 Martynenko, A., Shotton, K., Astatkie, T., Petrash, G., Fowler, C., Neily, W., Critchley, A.T.

513 (2016) Thermal imaging of soybean response to drought stress: the effect of *Ascophyllum*

514 *nodosum* seaweed extract. *Springerplus*, 5(1). doi: 10.1186/s40064-016-3019-2

515 Masuka, B., Araus, J.L., Das, B., Sonder, K., Cairns, J.E. (2012) Phenotyping for abiotic stress

516 tolerance in maize. *Journal of Integrative Plant Biology*, 54(4), 238-249. doi: 10.1111/j.1744-

517 7909.2012.01118.x.

- 518 MATLAB. (2018a). version 9.5.0 (R2018b). Natick, Massachusetts: The MathWorks Inc.
- 519 MATLAB. (2018b) Image Processing Toolbox Release R2018b, The MathWorks, Inc., Natick,  
520 Massachusetts, United States.
- 521 MATLAB. (2018c) Statistics and Machine Learning Toolbox Release R2018b, The MathWorks,  
522 Inc., Natick, Massachusetts, United States.
- 523 Meacham-Hensold, K., Montes, C.M., Wi, J., Guan, K., Fu, P., Ainsworth, E.A., Pederson, T.,  
524 Moore, C.E., Brown, K.L., Raines, C., Bernacchi, C.J. (2019) High-throughput field  
525 phenotyping using hyperspectral reflectance and partial least squares regression (PLSR) reveals  
526 genetic modifications to photosynthetic capacity. *Remote Sensing of Environment*, 231.  
527 doi:10.1016/j.rse.2019.04.029.
- 528 Moghimi, A., Yang, C., Miller, M.E., Kianian, S.F., Marchetto, P.M. (2018) A Novel Approach  
529 to Assess Salt Stress Tolerance in Wheat Using Hyperspectral Imaging. *Frontiers in Plant  
530 Science*, 9:1182. doi: 10.3389/fpls.2018.01182
- 531 Mohd Asaari, M.S., Mishra, P., Mertens, S., Dhondt, S., Inzé, D., Wuyts, N., Scheunders, P.  
532 (2018) Close-range hyperspectral image analysis for the early detection of stress responses in  
533 individual plants in a high-throughput phenotyping platform. *ISPRS Journal of Photogrammetry  
534 and Remote Sensing*, 138, 121-138. doi: 10.1016/j.isprsjprs.2018.02.003
- 535 Myles, S., Peiffer, J., Brown, P.J., Ersoz, E.S., Zhang, Z., Costich, D.E., Bluckler, E.S. (2009)  
536 Association Mapping: Critical Considerations Shift from Genotyping to Experimental Design.  
537 *The Plant Cell*, 21(8), 2194-2202. doi: 10.1105/tpc.109.068437

- 538 Obeidat, W., Avila, L., Earl, H., Lukens, L. (2018) Leaf Spectral Reflectance of Maize Seedlings  
539 and Its Relationship to Cold Tolerance. *Crop Science*, 58, 2569-2580. doi:  
540 10.2135/cropsci2018.02.0115
- 541 Pandey, P., Ge, Y., Stoerger, V., Schnable, J.C. (2017) High Throughput *In vivo* Analysis of  
542 Plant Leaf Chemical Properties Using Hyperspectral Imaging. *Front. Plant Sci.* 8:1348. doi:  
543 10.3389/fpls.2017.01348
- 544 Pantazi, X., Moshou, D., Bravo, C. (2016) Active learning system for weed species recognition  
545 based on hyperspectral sensing. *Biosystems Engineering*, 146, 193-202.  
546 doi:10.1016/j.biosystemseng.2016.01.014
- 547 Qiu, R., Yang, C., Moghimi, A. Zhang, M., Stefferson, B., Hirsch, C. (2019) Detection of  
548 Fusarium Head Blight in Wheat Using a Deep Neural Network and Color Imaging. *Remote*  
549 *Sensing*, 11(22), 2658. doi: 10.3390/rs11222658
- 550 R Core Team. 2012. R: A language and environment for statistical computing. R Foundation for  
551 Statistical Computing, Vienna, Austria. ISBN 3-900051-07-0, URL <http://www.R-project.org/>
- 552 Römer, C., Wahabzada, M., Ballvora, A., Pinto, F., Rossini, M., Panigada, C., Behmann, J.,  
553 Léon, J., Thureau, C., Bauckhage, C., Kersting, K., Rascher, U., Plümer, L. (2012) Early drought  
554 stress detection in cereals: simplex volume maximisation for hyperspectral image analysis.  
555 *Functional Plant Biology*, 39(11), 878-890. doi: 10.1071/FP12060
- 556 Rumpf, T., Mahlein, A., Steiner, U., Oerke, E., Dehne, H., Plümer, L. (2010) Early detection and  
557 classification of plant diseases with Support Vector Machines based on hyperspectral reflectance.

- 558 *Computers and Electronics in Agriculture*, 74(1), 91-99. doi: 10.1016/j.compag.2010.06.009
- 559 Silva-Perez, V., Molero, G., Serbin, S.P., Condon, A.G., Reynolds, M.P., Furbank, R.T., Evans,  
560 J.R. (2018) Hyperspectral reflectance as a tool to measure biochemical and physiological traits in  
561 wheat. *Journal of Experimental Botany*, 69(3), 483-496. doi: 10.1093/jxb/erx421
- 562 Singh, A., Ganapathysubramanian, B., Singh, A.K., Sarkar, S. (2016) Machine Learning for  
563 High-Throughput Stress Phenotyping in Plants. *Trends in Plant Science*, 21(2). doi:  
564 10.1016/j.tplants.2015.10.015
- 565 Smith, K.L., Steven, M.D., Colls, J.J. (2004) Use of hyperspectral derivative ratios in the red-  
566 edge region to identify plant stress responses to gas leaks. *Remote Sensing of Environment*,  
567 92(2), 207-217. doi: 10.1016/j.rse.2004.06.002
- 568 Thomas, S., Behman, J., Steier, A., Kraska, T., Muller, O., Rascher, U., Mahlein, A. (2018)  
569 Quantitative assessment of disease severity and rating of barley cultivars based on hyperspectral  
570 imaging in a non-invasive, automated phenotyping platform. *Plant Methods*, 14:45.  
571 doi:10.1186/s13007-018-0313-8
- 572 Varela, S., Assefa, Y., Prasad, P.V., Peralta, N.R., Griffin, T.W., Sharda, A., Ferguson, A., &  
573 Ciampitti, I.A. (2017) Spatio-temporal evaluation of plant height in corn via unmanned aerial  
574 systems. *Journal of Applied Remote Sensing*, 11(3). DOI: 10.1117/1.JRS.11.036013.
- 575 Watanabe, K., Guo, W., Arai, K., Takanashi, H., Kajiya-Kanegae, H., Kobayashi, M., Yano, K.,  
576 Tokunaga, T., Fujiwara, T., Tsutsumi, N., Iwata, H. (2017) High-Throughput Phenotyping of  
577 Sorghum Plant Height Using an Unmanned Aerial Vehicle and Its Application to Genomic

578 Prediction Modeling. *Front. Plant Sci.* 8:421. doi: 10.3389/fpls.2017.00421

579 Yendrek, C.R., Tomaz, T., Montes, C.M., Cao, Y., Morse, A.M., Brown, P.J., McIntyre, L.M.,

580 Leakey, A.D.B., Aisnworth, E.A. (2017) High-Throughput Phenotyping of Maize Leaf

581 Physiological and Biochemical Traits Using Hyperspectral Reflectance. *Plant Physiology*, 173,

582 614-626. doi:10.1104/pp.16.01447

583 Yoon, S.C., Park, B. (2015) Hyperspectral Image Processing Methods. In: Park B., Lu R. (eds)

584 Hyperspectral Imaging Technology in Food and Agriculture. Food Engineering Series. Springer,

585 New York, NY

586 Zhang, Q., Li, Q., Zhang, G. (2012) Rapid Determination of Leaf Water Content Using VIS/NIR

587 Spectroscopy Analysis with Wavelength Selection. *Journal of Spectroscopy*, 27. doi:

588 10.1155/2012/276795

## 589 **Data Statement**

590 All hyperspectral datasets are available through CyVerse. Scripts utilized for processing the

591 hyperspectral images as well as for leaf segmentation are available at

592 [https://github.com/SBTirado/HS\\_LeafSegmentation.git](https://github.com/SBTirado/HS_LeafSegmentation.git).

## 593 **Tables**

594 **Table S1. Summary of Experiments.**

595

Genotypes	Experiment	Day of Imaging	Treatments	Number of Plants per Genotype-Treatment-Day Combination	Total Number of Imaged plants
B73 Ki11 Mo17 MS71 Ph207	E1-Rep1	13 DAS	Control Cold: 6C day/2C night @ 11-13 DAS Heat: 39C day/29C night @ 11-13 DAS Salt: 50mL 0.75M NaCl @ 11 DAS	3	60
B73 Ki11 Mo17 MS71 Ph207	E1-Rep2	13 DAS	Control Cold: 6C day/2C night @ 11-13 DAS Heat: 39C day/29C night @ 11-13 DAS Salt: 50mL 0.75M NaCl @ 11 DAS	3	60
B73 Ki11 Mo17 MS71 Ph207	E1-Rep3	13 DAS	Control Cold: 6C day/2C night @ 11-13 DAS Heat: 39C day/29C night @ 11-13 DAS Salt: 50mL 0.75M NaCl @ 11 DAS	3	60
Mo17 Ph207	E2	11 DAS 13 DAS 15 DAS	Control 50mL 0.5M NaCl @ 11DAS 50mL 0.75M NaCl @ 11 DAS 50mL 1M NaCl @ 11 DAS	15	360
<b>Total Number of Plant Images</b>					540

596

## 597 **Figure Legends**

598 **Figure 1. Evaluating individual leaf segments. A)** Procedure for extracting hyperspectral data  
 599 from ten segments across the longest leaf of each plant. **B)** Mean (dark line) and variance in  
 600 reflectance of individual leaf segments, the entire longest leaf (all leaf segments combined) and  
 601 the entire plant of a Mo17 control plant at 13 days after sowing. Pixel counts represented in each  
 602 panel are indicated by the blue text. Leaf segment is indicated at the top of each panel in black  
 603 text.

604 **Figure 2. Reflectance of leaf segments across all Mo17 and PH207 control plants in**  
605 **experiment E2 at 15 days after sowing. A)** PCA biplots of the mean reflectance across all  
606 wavelengths of all 10 leaf segments for individual plants. Each datapoint constitutes an  
607 individual leaf segment for a single plant. **B)** Mean reflectance for the 10 leaf segments, the  
608 entire leaf and the entire plant. All plants were utilized to calculate the mean. Vertical black lines  
609 indicate wavelengths at 498 nm, 550 nm, and 625 nm. **C)** Distributions of the average reflectance  
610 per plant of leaf segments, the entire leaf, and the entire plant at 498 nm, 550 nm and 625 nm. **D)**  
611 Adjusted p-values from a pairwise wilcox test between pairwise comparisons of leaf segment,  
612 entire leaf (L), and whole plant (WP) reflectance, at 498 nm, 550 nm and 625 nm. Results were  
613 adjusted for multiple comparisons using the “holm” method. Black color indicates p-value <  
614 0.001.

615 **Figure 3. Reflectance of leaf segments across all PH207 control plants in experiment E2**  
616 **across 11, 13 and 15 days after sowing. A)** PCA biplots of the mean reflectance across all  
617 wavelengths of all 10 leaf segments for individual plants. Each datapoint constitutes an  
618 individual leaf segment for a single plant. **B)** Mean reflectance for the 10 leaf segments, the  
619 entire leaf and the entire plant. All plants were utilized to calculate the mean. Vertical black lines  
620 indicate wavelengths at 498 nm, 550 nm, and 625 nm. **C)** Distributions of the average reflectance  
621 per plant of leaf segments, the entire leaf, and the entire plant at 498 nm, 550 nm and 625 nm  
622 across the three days of imaging.

623 **Figure 4. Genotypic differences in hyperspectral profiles for all control plants of each**  
624 **genotype in Experiment E1. A)** Average reflectance values across all control plants of each  
625 genotype. **D)** Average proportion of pixels per plant from all plants of a certain genotype (rows)

626 for each leaf segment (columns) predicted to belong to a certain genotypic class. Error bars  
627 indicate the standard deviation in pixel values from the mean.

628 **Figure 5. Proportion of pixels per plant classified as being salt stressed based on cubic**  
629 **SVM model developed from the wavelengths in the visible range of the spectrum and**  
630 **genotype as the predictor variables and using the medium salt stress and control**  
631 **treatments as the response variables. A)** Three salt treatments were applied after imaging at 11  
632 days after sowing (DAS). Plants were then imaged at 13 and 15 DAS. Reflectance values were  
633 calculated for entire plants, entire leaves and individual leaf segments. **B)** Proportion of total  
634 pixels for each plant across treatments in Experiment E2 classified as belonging to the salt stress  
635 category for the model developed using pixels across the whole plant. **C)** Proportion of total  
636 pixels for individual leaf segments and the entire leaf per plant for Mo17 classified as belonging  
637 to the salt stress category for a model developed using pixels across individual plant segments  
638 with segment number as a predictor variable.

639 **Figure 6. Differences in hyperspectral profiles across treatments for all Ki11 and Mo17**  
640 **plants in Experiment E1. A)** Average reflectance values for all plants in the cold, control, heat  
641 and salt stress treatments of Ki11 and Mo17 in Experiment E1. **B)** Average proportion of pixels  
642 from all Ki11 plants of a certain treatment (rows) for each leaf segment (columns) predicted to  
643 belong to a certain treatment class. Bars represent the mean proportion of all plants per category  
644 and error bars represent the standard deviation around the mean. **C)** Average proportion of pixels  
645 from all plants of a certain treatment (rows) for genotypes across selected leaf segments  
646 predicted to belong to a certain treatment class. Bars represent the mean proportion of all plants  
647 per genotype and treatment class predicted to belong to a certain treatment.

648 **Supplemental Figure Legends**

649 **Figure S1. Hyperspectral imaging setup. A)** Imaging system utilized. **B)** RGB representation  
650 of staged plants **C)** Sensor and light configuration.

651 **Figure S2. Variation in reflectance measurements among pixels within whole plants.**

652 Standard deviation of pixel reflectance values across whole plants for three (A, B and C) Mo17  
653 and PH207 control plants from a single plot imaged at the indicated day after sowing (DAS).  
654 Black line indicates reflectance at 625 nm.

655 **Figure S3. Mean RGB trait values for all PH207 control plants in experiment E2 across 11,**  
656 **13 and 15 days after sowing (DAS).**

657 **Figure S4. RGB images for one representative plant in experiment E1 for each treatment**  
658 **for Ki11 and Mo17 genotypes 13 days after sowing.**

659 **Figure S5.** Average proportion of pixels from all Mo17 (**A**) and B73 (**B**) plants of a certain  
660 treatment (rows) for each leaf segment (columns) predicted to belong to a certain treatment class.  
661 Bars represent the mean proportion of all plants per category and error bars represent the  
662 standard deviation around the mean.

663 **Figure S6.** Average proportion of pixels from all MS71 (**A**) and PH207 (**B**) plants of a certain  
664 treatment (rows) for each leaf segment (columns) predicted to belong to a certain treatment class.  
665 Bars represent the mean proportion of all plants per category and error bars represent the  
666 standard deviation around the mean.

667 **Figure S7. SVM model training and testing procedure.**

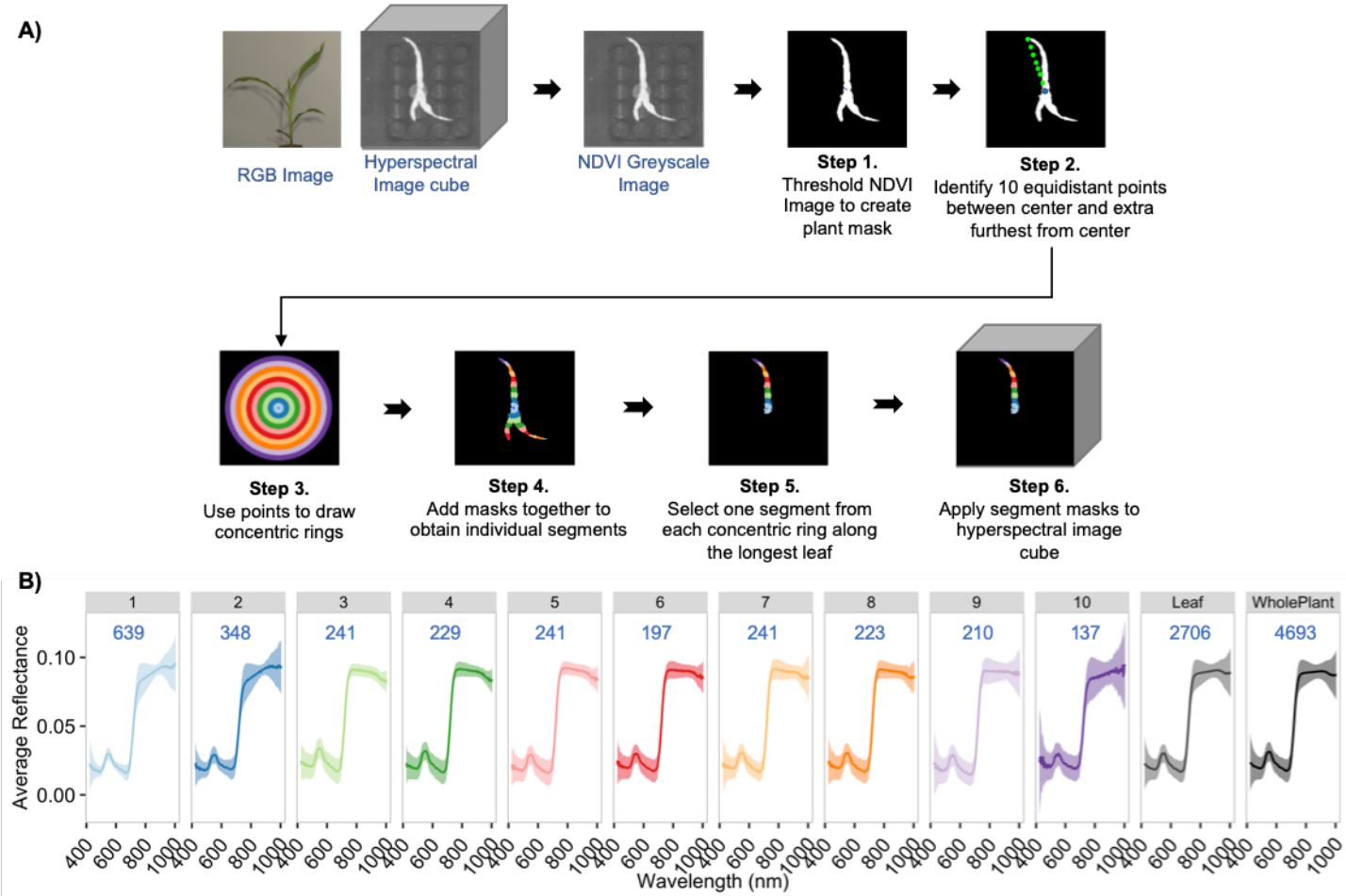


**Figure 1. Evaluating individual leaf segments. A)** Procedure for extracting hyperspectral data from ten segments across the longest leaf of each plant. **B)** Mean (dark line) and variance in reflectance of individual leaf segments, the entire longest leaf (all leaf segments combined) and the entire plant of a Mo17 control plant at 13 days after sowing. Pixel counts represented in each panel are indicated by the blue text. Leaf segment is indicated at the top of each panel in black text.

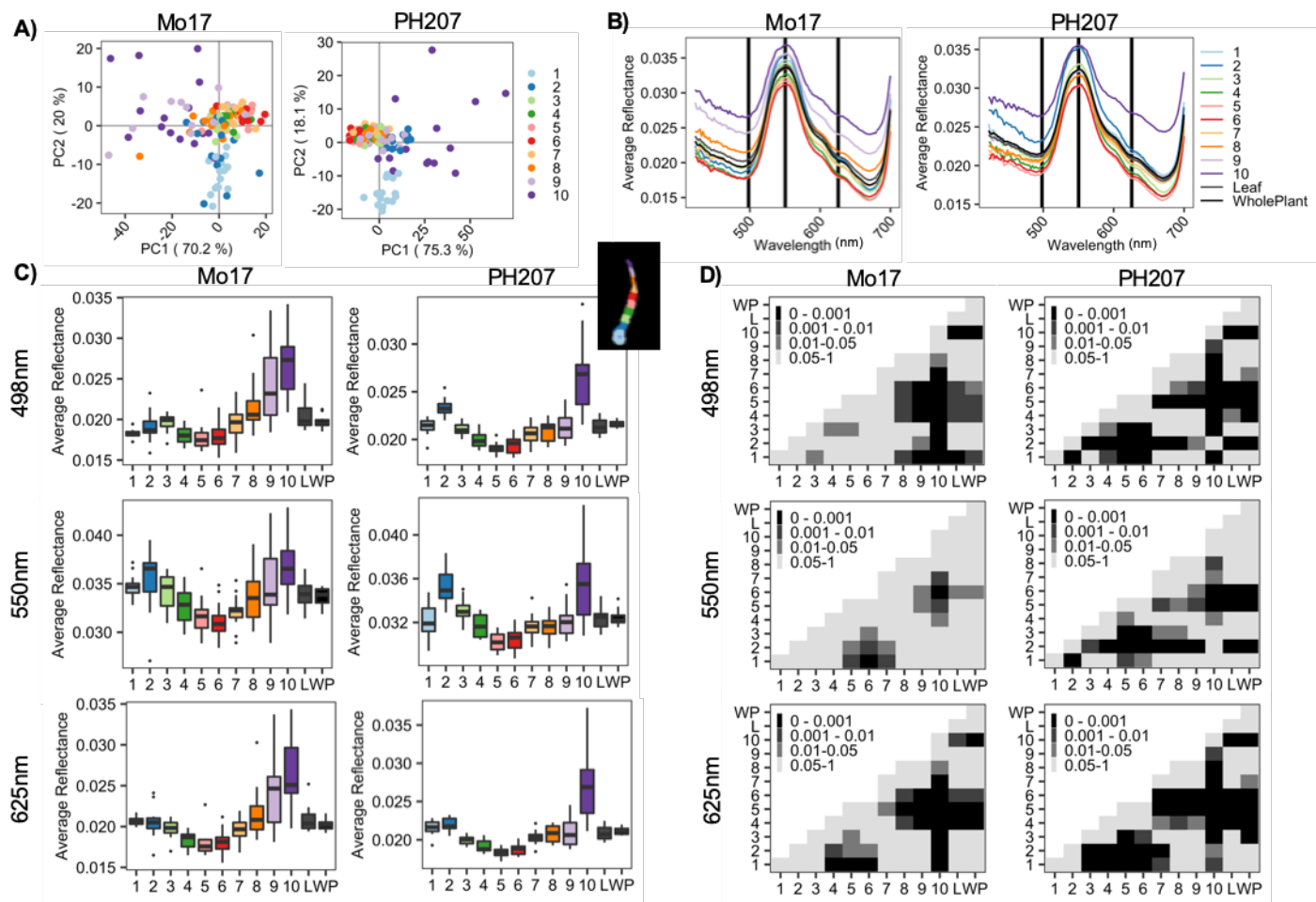


**Figure 2. Reflectance of leaf segments across all Mo17 and PH207 control plants in experiment E2 at 15 days after sowing.** **A)** PCA biplots of the mean reflectance across all wavelengths of all 10 leaf segments for individual plants. Each datapoint constitutes an individual leaf segment for a single plant. **B)** Mean reflectance for the 10 leaf segments, the entire leaf and the entire plant. All plants were utilized to calculate the mean. Vertical black lines indicate wavelengths at 498 nm, 550 nm, and 625 nm. **C)** Distributions of the average reflectance per plant of leaf segments, the entire leaf, and the entire plant at 498 nm, 550 nm and 625 nm. **D)** Adjusted p-values from a pairwise wilcox test between pairwise comparisons of leaf segment, entire leaf (L), and whole plant (WP) reflectance, at 498 nm, 550 nm and 625 nm. Results were adjusted for multiple comparisons using the “holm” method. Black color indicates p-value < 0.001.

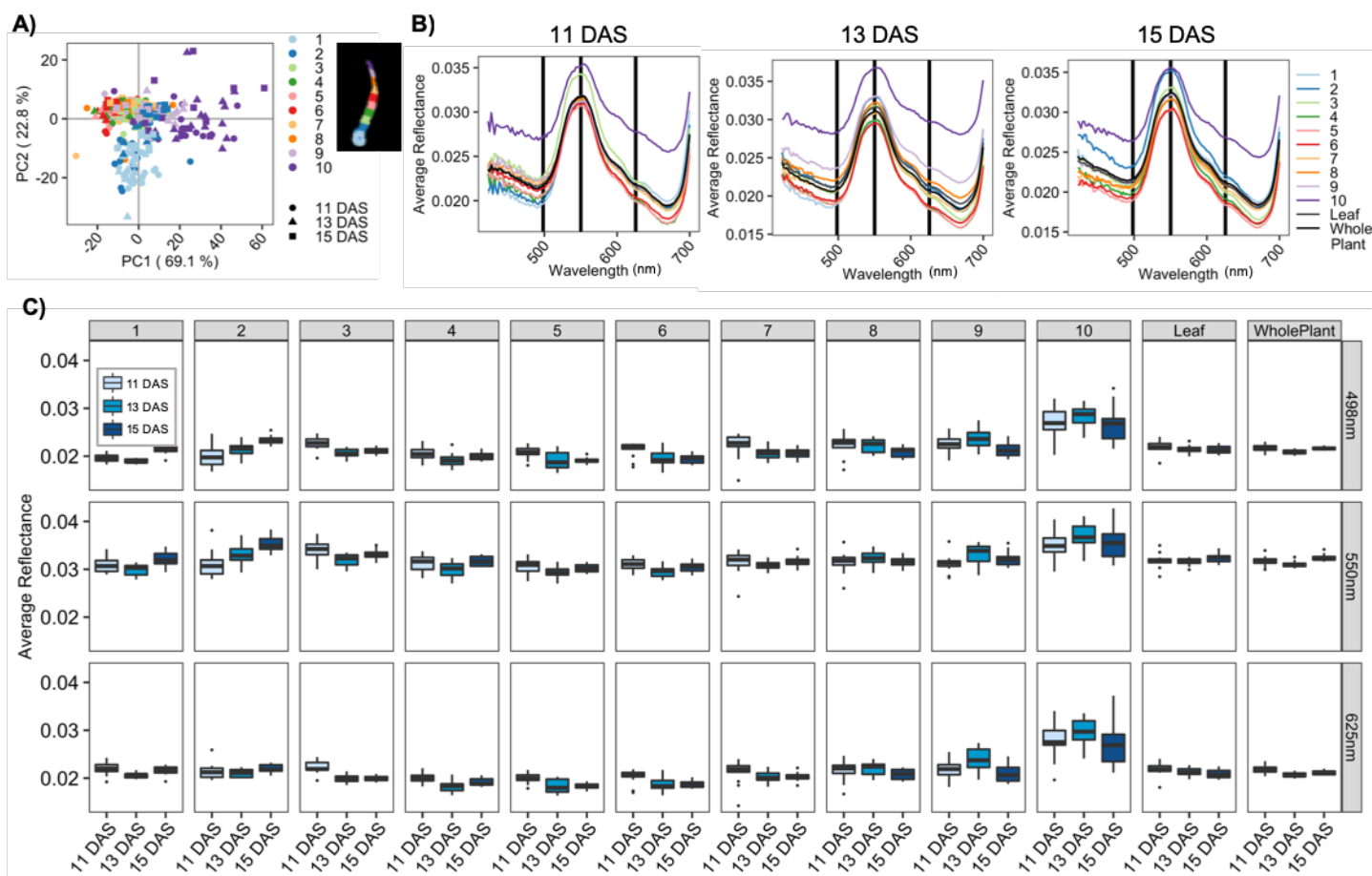


**Figure 3. Reflectance of leaf segments across all PH207 control plants in experiment E2 across 11, 13 and 15 days after sowing. A)** PCA biplots of the mean reflectance across all wavelengths of all 10 leaf segments for individual plants. Each datapoint constitutes an individual leaf segment for a single plant. **B)** Mean reflectance for the 10 leaf segments, the entire leaf and the entire plant. All plants were utilized to calculate the mean. Vertical black lines indicate wavelengths at 498 nm, 550 nm, and 625 nm. **C)** Distributions of the average reflectance per plant of leaf segments, the entire leaf, and the entire plant at 498 nm, 550 nm and 625 nm across the three days of imaging.

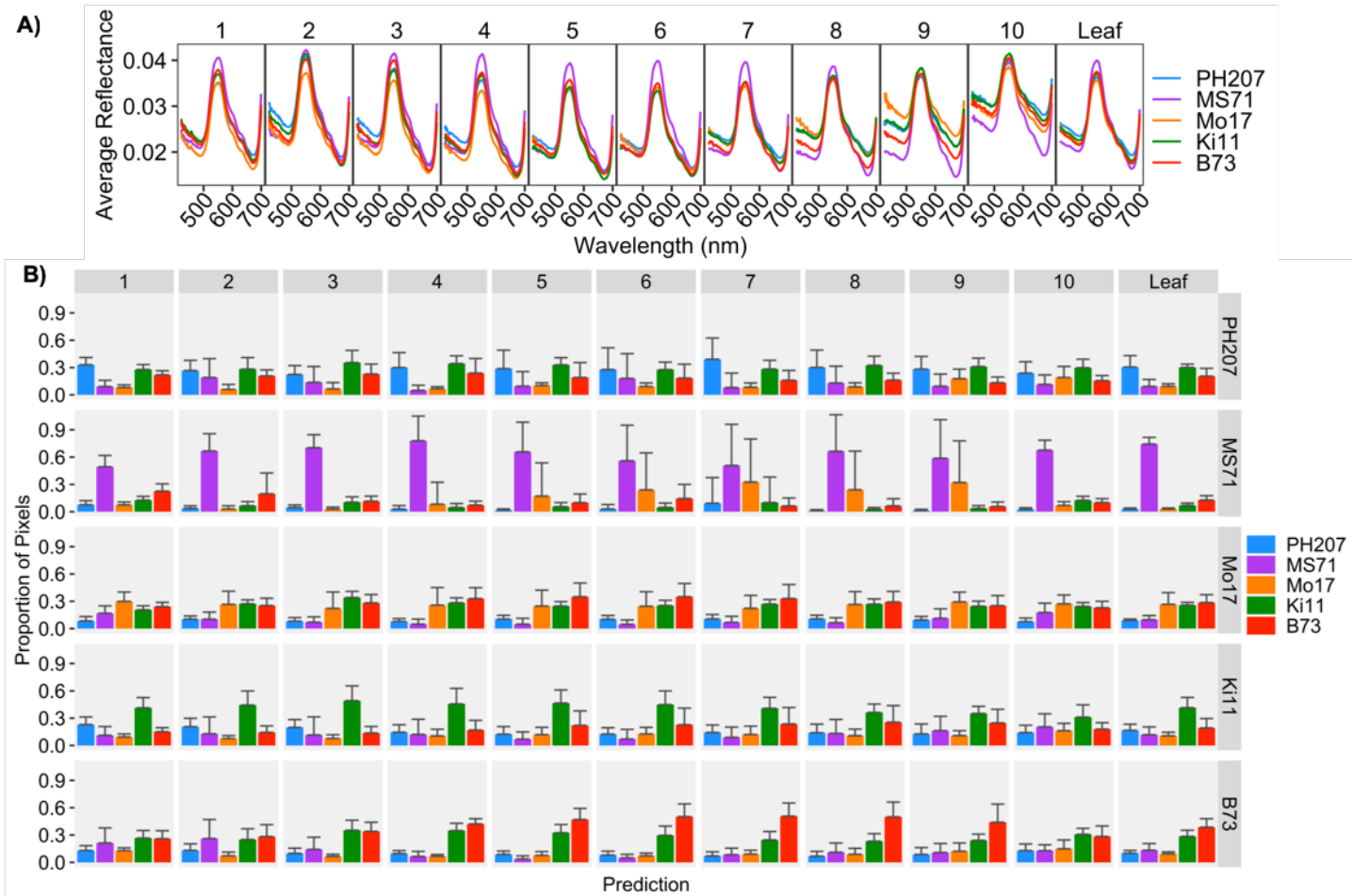


**Figure 4. Genotypic differences in hyperspectral profiles for all control plants of each genotype in Experiment E1. A)** Average reflectance values across all control plants of each genotype. **D)** Average proportion of pixels per plant from all plants of a certain genotype (rows) for each leaf segment (columns) predicted to belong to a certain genotypic class. Error bars indicate the standard deviation in pixel values from the mean.

